Evidence of the Ion Cyclotron Resonance at Proton Kinetic Scales in the Solar Wind

Roberts, Owen; Li, Xing

Published in:
Astrophysical Journal

DOI:
10.1088/0004-637X/802/1/1

Publication date:
2015

Citation for published version (APA):
Roberts, O., & Li, X. (2015). Evidence of the Ion Cyclotron Resonance at Proton Kinetic Scales in the Solar Wind. *Astrophysical Journal*, *802*(1), 1-11. https://doi.org/10.1088/0004-637X/802/1/1

The Astrophysical Journal, 802:1 (11pp), 2015 March 20 doi:10.1088/0004-637X/802/1/1

EVIDENCE OF THE ION CYCLOTRON RESONANCE AT PROTON KINETIC SCALES IN THE SOLAR WIND

O. W. Roberts and Xing Li
Department of Physics, Aberystwyth University, Aberystwyth, Ceredigion SY23 3BZ, UK; o.wyn.roberts@gmail.com, xxl@aber.ac.uk
Received 2014 August 15; accepted 2014 December 25; published 2015 March 13

ABSTRACT

The k-filtering and wave polarization techniques are applied to Cluster magnetic field data at four intervals of fast free (not connected to Earth's foreshock) solar wind. In addition to the commonly observed population of magnetic field fluctuations propagating at quasi-perpendicular angles to the global mean field $\mathbf{B_0}$, a population of fluctuations propagating at quasi-parallel angles are also observed when no local plasma instability can be identified. At low wavenumbers ($kv_A/\Omega_p \leqslant 0.6$) both components are present, and have powers of similar strength, while at higher wavenumbers ($kv_A\Omega_p > 0.6$) only the perpendicular component can be identified. Here v_A and Ω_p are the Alfvén speed and the proton (angular) gyration frequency, k denotes the wavenumber. The dispersion curve obtained (and the ratio of the magnitudes of left and right hand polarized fluctuations) shows a sharp transition (and decrease) at $(kv_A/\Omega_p) \sim 0.6$, which corresponds to a spacecraft frequency $f_{sc} = 0.32$ Hz. At higher wavenumbers the measurements agree with previous studies indicating the presence of kinetic Alfvén wave (KAW) turbulence or a mixture of KAW turbulence and convected structures. The parallel component displays a scaling of $k_{\parallel}^{-\delta}$ where the spectral index δ ranges between about $5/3$ and 2 although the number of data points does not warrant an accurate determination. The origins of the observed parallel component are unclear. The presence of a parallel component is consistent with ion cyclotron waves, and we interpret the sharp drop of this component at higher wavenumbers as evidence that the ion cyclotron resonance is occurring in the solar wind intervals studied.

Key words: solar wind – turbulence – waves

1. INTRODUCTION

The solar wind is a highly turbulent plasma outflowing from the Sun, and the exact heating and acceleration mechanisms remain unclear (Tu & Marsch 1995; Bruno & Carbone 2013). At large scales (where magnetohydrodynamics is valid) MHD Alfvén waves dominate and are ubiquitously observed in the fast solar wind (Belcher 1971) although they experience a depletion with increasing heliocentric distance (Bruno et al. 2003). A local turbulent cascade ensues preferentially in the direction perpendicular to the mean magnetic field, introducing a strong anisotropy such that $k_\perp \gg k_\parallel$ (Shebalin et al. 1983; Matthaeus et al. 1990; Goldreich & Sridhar 1995). The nonlinear cascade produces an energy spectrum that includes an energy injection scale, an inertial range, and a possible ion dissipation range (Bruno & Carbone 2013) and the turbulent cascade continues to operate at ever smaller scales, up to electron gyroradius (Alexandrova et al. 2009; Alexandrova et al. 2012; Chen et al. 2013; Sahraoui et al. 2013). After the inertial range there is a spectral break at the ion inertial length or the ion Larmor radius (Bourouaine et al. 2012), and a steepening in the spectrum to a scaling that is observed to vary between -3.75 and -1.75 (Alexandrova et al. 2012; Bruno et al. 2014). This is often termed the ion dissipation or ion dispersion range in literature. One interpretation used to explain the strong anisotropy at these scales is that there is a cascade of oblique waves, with kinetic Alfvén waves (KAWs) being suggested by observations (Sahraoui et al. 2010b; He et al. 2012a; Salem et al. 2012; Chen et al. 2013; Roberts et al. 2013; see also a review of the observational evidence Podesta 2013). The other interpretation is that these scales are populated with oblique whistler waves (Biskamp et al. 1996; Stawicki et al. 2001; Li et al. 2001; Gary & Smith 2009) with some observational support in the solar wind (Neubauer et al. 1977; Coroniti et al. 1982; Lengyel-Frey et al. 1996). Other alternatives could be plasma coherent structures, such as magnetic vortices, shocks, or current sheets (Bruno et al. 2003; Perri et al. 2012; Roberts et al. 2013). However, the exact contributions of these various ideas to the acceleration and heating of the solar wind remain to be demonstrated.

In the direction parallel to the magnetic field the cascade is less efficient according to critical balance turbulence theory (Goldreich & Sridhar 1995, 1997) and it has been identified in hybrid-Vlasov simulations (Verscharen et al. 2012). However, it remains difficult to identify definitively in the solar wind. This has led to the question of whether a parallel cascade exists at all. While the majority of work has focused on the perpendicular component, there is some evidence of parallel propagating magnetic waves (Jian et al. 2009, 2010) or fluctuations (He et al. 2011; Podesta & Gary 2011) at ion kinetic scales in the solar wind. Two recent studies of the magnetic helicity (He et al. 2011; Podesta & Gary 2011) demonstrated the presence of a quasi parallel component coexisting with a perpendicular component. This signature could be due to anti-sunward ion cyclotron waves, or sunward parallel whistler waves, generated either from a parallel cascade (He et al. 2011, 2012b), or as the result of a plasma temperature anisotropy instability (Gary et al. 1976; Podesta & Gary 2011; Klein et al. 2014).

Ion cyclotron waves (ICWs) have been an exciting explanation of ion heating in the solar wind. These waves are the continuation of the Alfvén wave at high frequencies close to the proton gyration frequency. This can lead to efficient transfer of energy between the wave and the particle through cyclotron resonance. In the past decades, extensive studies of ICWs have been performed (Tu & Marsch 1997; Li & Habbal 1999; Hollweg & Isenberg. 2002; Cranmer. 2014) to explain the preferential heating of heavy ions in the solar corona, and the large perpendicular temperatures observed in the solar corona (Kohl et al. 1998; Li et al. 1998, see also the extensive review by Antonucci et al. 2012). Anisotropies in the velocity distribution function were also investigated by Telloni et al. (2007) and were attributed to ion cyclotron resonant scattering. They have also been frequently observed in relation to ion pickup at planetary

bodies (e.g., Glassmeier & Neubauer 1993), but have rarely been seen in the solar wind. However, they have been observed in the solar wind at 1 AU (Jian et al. 2009) and closer to the Sun at 0.3 AU (Jian et al. 2010). These studies suggest that the ICWs are generated in an upstream region due to the lack of a correlation with a local field (Jian et al. 2010). It is also suggested that these have been difficult to detect since they typically exist for a short period of time <60 s, and are usually much smaller than the total length of intervals studied. Recently a study of the location of the spectral break between the inertial and dissipation ranges concluded that cyclotron resonant interactions (Bruno & Trenchi 2014) must participate in the cascade. This study found that the wavenumber at the spectral break corresponded best to the resonant condition for parallel Alfvén waves.

Unfortunately, observations of the solar wind are typically limited to a single spacecraft that leaves us unable to distinguish between spatial and temporal changes, and are thus reliant on Taylor's hypothesis (Taylor 1938). This may not be satisfied in the solar wind (Perri et al. 2010) especially when the flow speed is very low, waves are very dispersive, or fluctuation amplitudes are large (Howes et al. 2014; Klein et al. 2014). Using Taylor's hypothesis, one would often assume that the wavevector follows the direction of the solar wind flow. However, this can lead to significant uncertainties (Sahraoui et al. 2010b; Roberts et al. 2013). One technique that does not invoke Taylor's hypothesis is the *k*-filtering technique (Pinçon & Lefeuvre 1991), which assumes that the turbulent fluctuations can be described as a superposition of plane waves with random phases, and has been validated for a signal that consists of a combination of random phase plane waves, and non-random phase coherent structures (Roberts et al. 2014; Roberts 2014).

Application of the *k*-filtering method to the solar wind is not a trivial task, and the applications have produced different results and interpretations. This may be in part due to different plasma conditions sampled, different spacecraft geometries, and some intervals being contaminated with backstreaming particles from the foreshock. For a more complete discussion of these results the reader is referred to Roberts et al. (2014b). Sahraoui et al. (2010b) found that KAW turbulence in the ion kinetic scale describes the observations well, while the parallel component is too weak, and errors too large for distinct identification. Roberts et al. (2013) conclude that turbulence at the ion kinetic scale is consistent with the presence of kinetic Alfvén waves and static structures being advected over the spacecraft. Narita et al. (2011) and Perschke et al. (2013) suggest that linear Vlasov theory cannot describe the turbulence due to the large frequency spread observed, and find weak agreement with the curves for whistler waves. All of these studies agree that turbulence is highly anisotropic at the MHD and ion kinetic scales: the propagation angles that the wavevector makes with the global mean field are such that $\theta_{\mathbf{kB_0}} \sim 90^\circ \pm 10^\circ$.

In this paper we present a new study using the *k*-filtering method, where we are able to identify a population of quasi-parallel propagating magnetic fluctuations at small wavenumbers ($0.1 < (kv_A/\Omega_p) \leqslant 0.6$), with a maximum frequency in the plasma frame of around $(\omega/\Omega_p) \sim 0.7$ which is enough to satisfy the ion cyclotron resonance condition for protons in a plasma with plasma beta ~1:

$$\omega - k_\parallel v_\parallel - \Omega_p = 0, \quad (1)$$

and can lead to substantial heating in the direction perpendicular to the magnetic field. Close inspection of the three dimensional power spectral density $P(\omega_{sc}, \mathbf{k})$ shows that both a parallel and a perpendicular component of the magnetic fluctuations are present. The parallel component is dominant at small wavenumbers. At higher wavenumbers (or frequencies) the highly oblique nature of the turbulence is recovered in accordance with previous applications of the *k*-filtering method. We also investigate the polarization of these fluctuations in the plane perpendicular to the wavevector obtained from *k*-filtering (Roberts et al. 2013). We will discuss the possible reasons why previous *k*-filtering studies have been unable to recover this component. In Section 2 the data will be presented and the analysis methods discussed, in Section 3 the results will be presented, followed by a discussion and a conclusion.

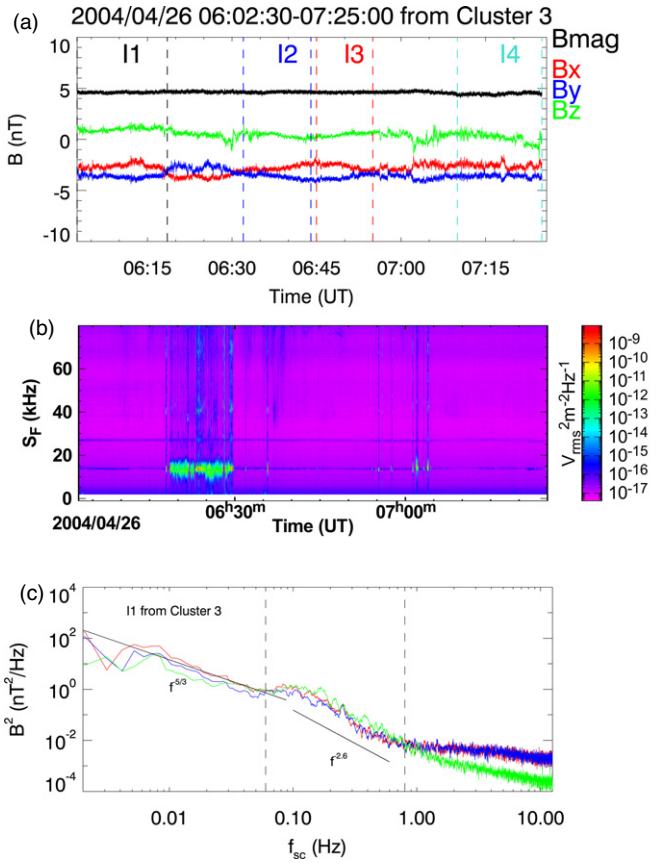

Figure 1. (a) Raw magnetic field time series in GSE coordinates and the magnitude. The vertical lines denote the time intervals. (b) E-field natural spectrogram from the WHISPER instrument (Décréau et al. 2001). Intervals are chosen such that noisy periods in this are not included in the *k*-filtering analysis. (c) Fourier power spectra of interval 1.

2. DATA AND ANALYSIS

Magnetic field data is obtained from the fluxgate magnetometer Balogh et al. (2001) on the Cluster spacecraft (Escoubet et al. 2001). Full resolution data is available with a sampling rate of 22 s^{-1} and spin resolution plasma data (4 s) is available from the Hot Ion Analyzer (HIA) which is one of the two plasma instruments of the Cluster Ion Spectrometer instrument (CIS; Reme et al. 2001) on C1 and C3. The raw magnetic field data from C3 is shown in Figure 1(a): the vertical lines denote the time intervals analyzed, the three components of the magnetic field and the magnitude is also plotted. Intervals are chosen such that there are no shocks or discontinuities and there are no large trends. As a result, the signals satisfy the requirement of weak stationarity, and spatial homogeneity (Matthaeus &

Table 1
Mean Plasma and Spacecraft Parameters in the Intervals Studied

	I1 26 Apr 06:02:30-06:18:30 2004	I2 26 Apr 06:32:00-06:44:00 2004	I3 26 Apr 06:45:00-06:55:30 2004	I4 26 Apr 07:10:00-07:25:00 2004
$B\ (nT)$	4.6	4.6	4.6	4.4
$\sigma_{\rm Bdir}(^\circ)$	6.1	3.8	4.1	4.0
$\sigma_{\rm Bmag}(nT)$	0.08	0.09	0.08	0.10
$n\ ({\rm cm}^{-3})$	2.2	2.2	2.2	2.3
β	0.95	1.00	0.88	0.98
$V_{\rm sw}({\rm km\ s}^{-1})$	496	494	495	489
$\sigma_v({\rm km\ s}^{-1})$	11	10	11	10
$f_{\rm ci}$	0.071	0.071	0.071	0.068
v_A	68.4	67.8	68.3	64.9
E	0.02	0.01	0.01	0.03
P	0.02	0.02	0.04	0.06
$\theta_{\mathbf{VB_0}}$	61.1	60.4	61.8	61.9
$T_{i\perp}/T_{i\parallel}$	1.18	1.2	1.3	1.3
ρ_i (km)	163	167	166	174
d_i (km)	152	151	154	151

Goldstein 1982). The Fourier power spectrum of the magnetic field fluctuations is plotted in Figure 1(b). Rather than directly calculating the power spectrum $P_i(f)$ of the magnetic field, the power spectrum $P_i^\Delta(f)$ of the differences $\Delta\mathbf{B} = \mathbf{B}(t+\delta t) - \mathbf{B}(t)$ is calculated. The amplitude is then corrected by applying a post darkening filter as follows.

$$P_i(f) = \frac{P_i^\Delta(f)}{4\sin^2(\pi f \delta t)}, \quad (2)$$

where i is x, y or z direction. This technique amounts to "pre-whitening" and "post-darkening" the spectrum as described by Bieber et al. (1993) and has the advantage of limiting spectral leakage at lower frequencies. The vertical lines denote the frequency region where we apply the k-filtering method. The lower and upper frequency limits are at 0.06 Hz and 0.8 Hz. The lower limit was chosen so that we can determine k with a greater accuracy than 10%. This corresponds to a $k = k_{\rm max}/25$ (Sahraoui et al. 2010a). The upper limit was chosen to avoid the flattening we see at $\sim$ 0.9–1.0 Hz in Figure 1(c). The electric field spectrogram shown in Figure 1(c) is quiet in the subintervals studied indicating that the spacecraft is in the free solar wind, and are not magnetically connected to the bow shock (Etcheto & Faucheux 1984; Lacombe et al. 1985). The average plasma and spacecraft parameters are given in Table 1, with $\sigma_{\rm Bdir}$ denoting the standard deviation of the direction of the magnetic field vector in degrees, and $\sigma_{\rm Bmag}$ and σ_v denoting the standard deviations of the magnitude of the magnetic field and solar wind velocity, respectively. The ion density is n, the ion plasma beta is β, the solar wind speed is $V_{\rm sw}$, and the proton gyration frequency is $f_{\rm ci}$. The ion temperature anisotropy is $T_{i\perp}/T_{i\parallel}$ where $T_{i\perp}$ and $T_{i\parallel}$ are the ion temperatures in directions perpendicular and parallel to the mean magnetic field. The proton gyroradius and inertial length are $\rho_i = (2k_B T_{i\perp}/m_p\Omega_p)$ and $d_i = v_A/\Omega_p$, respectively. The proton mass is m_p and the Boltzmann constant is k_B. The Cluster configuration parameters "Elongation" and "Planarity" that describe the degree to which the four Cluster spacecraft are close to a perfect tetrahedron (Robert et al. 1998), are denoted by "E" and "P," and are very close to zero indicating a geometry close to that of a perfect (regular) tetrahedral configuration. Low values of these parameters are required so that no unphysical anisotropy is introduced due to lack of homogeneous sampling in space (Sahraoui et al. 2010a).

The velocity of the intervals studied is high $v_{\rm sw} \sim 500\,{\rm km\,s}^{-1}$, and the density is low $\sim$2 cm^{-3}. This suggests that these intervals can be best classified as being representative of the *fast* wind.

The k-filtering method is applied to the magnetic field data from the four Cluster spacecraft. Using k-filtering we are able to determine the power spectral density $P(\omega_{\rm sc}, \mathbf{k})$. We analyze this in two ways: we consider the maximum in the spectrum and its location in the wavenumber space, and we consider the full spectrum and its three-dimensional morphology.

The k-filtering technique is based on Fourier analysis and is subject to a well known spatial aliasing effect due to the periodic nature of sine or cosine functions. While it is impossible to completely eliminate this effect we can take steps to minimize contributions that could be from spatial aliasing. A maximum wavevector is defined as $k_{\rm max} = (\pi/d_{\rm min})$ (Sahraoui et al. 2010a; Roberts et al. 2013), which also sets a maximum spacecraft frequency $f_{\rm max}$. The data are from 2004 when the Cluster spacecraft had a minimum separation $d_{\rm min} \sim 200$ km allowing the investigation of both ion inertial and dissipation ranges. A parallelepiped in wavenumber space is also defined from spacecraft geometry (Tjulin et al. 2005) and any maxima found outside are assumed to be due to aliasing effects and are removed from further analysis. In the spacecraft frame the maximum frequency is $k_{\rm max}(V_{\rm sw} - v_{ph})/(2\pi)$ and in the solar wind frame the maximum frequency is $k_{\rm max}v_{ph}/(2\pi)$, where v_{ph} is the phase speed of a possible plasma wave. This is trivial for KAWs since the phase speed of KAWs is generally much smaller than the solar wind speed. However, if we anticipate whistler waves that have much larger phase speeds, we must adjust our limitations in frequency to reflect this (Sahraoui et al. 2010a). In this work we chose $v_{ph} = v_A$. A minimum wavenumber is chosen as $k_{\rm max}/25$ such that the wavevector can be determined with accuracy better than 10% (Sahraoui et al. 2010a).

The studies that have used k-filtering in the solar wind have been unable to resolve a parallel component, possibly because the method may be biased to recover the more powerful perpendicular fluctuations, especially when we only consider the maximum in $\mathbf{k}$ space. A key limitation of k-filtering is due to the chosen orientation of the magnetic field vector with respect

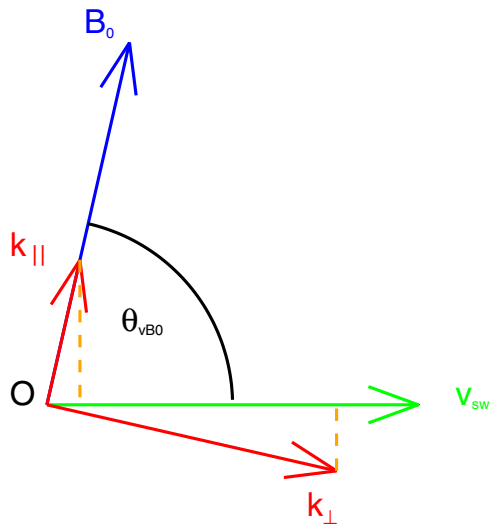

Figure 2. Schematic of the geometry of the magnetic field vector (blue), solar wind velocity (green), the parallel and perpendicular components of the wavevector (red), and the angle $\theta_{\mathbf{vB_0}}$ (black). The orange dashed lines show the minimum distance from the parallel and perpendicular components of the wavevector to the velocity vector. The projection of the wavevectors onto the velocity vector would be given by the line from the origin O to the orange lines along $\mathbf{v}_{\rm sw}$.

to the velocity vector to avoid contamination of backstreaming particles from the bow shock (X. Li et al. 2015, in preparation). When the Cluster spacecraft is in the solar wind, its orbit keeps it close to the Earth's foreshock. In order to avoid magnetic connection with the foreshock, intervals of solar wind are often selected with $\theta_{\mathbf{vB_0}} > 60^\circ$ as a minimum requirement. If we consider a wavevector that is made up of a perpendicular and parallel (to the mean magnetic field) component $\mathbf{k} = \mathbf{k}_\parallel + \mathbf{k}_\perp$, then in this scenario with $\theta_{\mathbf{vB_0}} \sim 90^\circ$, the projection of the parallel component onto the solar wind velocity direction will be close to zero, making an already small parallel component's projection onto the velocity vector even smaller. Figure 2 shows a diagram of the situation, where $\theta_{\mathbf{vB_0}} > 60^\circ$, and it clearly shows that the projection of the parallel component of the wavevector onto the solar wind velocity direction very very small (the distance between the origin O to the orange dashed lines) compared to that of the perpendicular component at the given geometry. If the Cluster was further from the foreshock and magnetic connection was not an issue, we would be able to analyze intervals where the angle $\theta_{\mathbf{vB_0}}$ is smaller and the projection of the parallel component is much larger.

In order to maximize our chances of recovering the parallel component, we analyze data where the angle between the magnetic field and the bulk velocity is close to 60°. By considering the three-dimensional shape of $P(\omega_{\rm sc}, \mathbf{k})$, we are able to resolve two components at comparable powers.

3. RESULTS

The angles between the wavevector at maximum power with respect to the global mean field $\mathbf{B_0}$ are shown in Figure 3 and in contrast to previous studies that adopted the k-filtering technique, there is a quasi-parallel propagating component with $0^\circ < \theta_{\mathbf{kB_0}} < 40^\circ$ from low frequencies up to a spacecraft frequency $f_{\rm sc} \sim 0.32$ Hz ($kv_A/\Omega_p \sim 0.6$), above which the magnetic fluctuations return to the familiar quasi-perpendicular propagation with $\theta_{\mathbf{kB_0}} \sim 90^\circ$ (Sahraoui et al. 2010b; Narita et al. 2011; Roberts et al. 2013; Perschke et al. 2013; Roberts 2014). A table of the mean values of the angles is given in Table 2. An interesting feature of the plot is that the parallel component exhibits a sharp cutoff at $(kv_A/\Omega_p) \sim 0.6$ which could signify that damping due to kinetic effects has kicked in at these scales. It should be noted that these results do not contradict previous studies since the parallel component may be present in those studies, but may have significantly smaller power than the perpendicular component, and are also mitigated by the projection effect. However, most intervals analyzed in both the fast and slow solar wind show that the angles at all scales are highly oblique (see the companion paper by Roberts et al. 2014b, and Roberts 2015).

Table 2
Table of Angle Results for Fast Wind Cases Studied

	I1	I2	I3	I4
$\langle\theta_{\mathbf{kB_0}}\rangle$ $\frac{kv_A}{\Omega_p} < 0.62$	21.7	36.1	36.8	20.2
$\langle\sigma_{\theta_{\mathbf{kB_0}}}\rangle$ $\frac{kv_A}{\Omega_p} < 0.62$	11.0	11.5	11.0	10.6
$\langle\theta_{\mathbf{kB_0}}\rangle$ $\frac{kv_A}{\Omega_p} > 0.62$	82.3	82.8	76.6	85.9
$\langle\sigma_{\theta_{\mathbf{kB_0}}}\rangle$ $\frac{kv_A}{\Omega_p} > 0.62$	8.2	7.6	8.4	8.0
$\langle\theta_{\mathbf{kv_{sw}}}\rangle$ $\frac{kv_A}{\Omega_p} < 0.62$	51.1	30.0	45.4	44.2
$\langle\sigma_{\theta_{\mathbf{kv_{sw}}}}\rangle$ $\frac{kv_A}{\Omega_p} < 0.62$	10.2	10.8	10.1	10.6
$\langle\theta_{\mathbf{kv_{sw}}}\rangle$ $\frac{kv_A}{\Omega_p} > 0.62$	24.5	29.8	32.3	27.8
$\langle\sigma_{\theta_{\mathbf{kv_{sw}}}}\rangle$ $\frac{kv_A}{\Omega_p} > 0.62$	6.9	6.6	7.3	6.9

In order to investigate some of these frequencies further we analyze selected frequencies from the first interval (I1). The full three-dimensional power spectral density at sampling frequency 0.066 Hz and 0.591 Hz determined by the k-filtering technique is given in Figures 4(a) and (b). The surfaces denote areas of constant power, and the axes are given by

$$k_\parallel = \mathbf{k}\cdot\mathbf{e}_x, k_{\perp 1} = \mathbf{k}\cdot\mathbf{e}_y, k_{\perp 2} = \mathbf{k}\cdot\mathbf{e}_z \quad (3)$$

where

$$\mathbf{e}_x = \mathbf{B_0}/B_0, \mathbf{e}_z = \mathbf{V}_{\rm sw}\times\mathbf{B}_0/|\mathbf{V}_{\rm sw}\times\mathbf{B}_0|, \mathbf{e}_y = \mathbf{e}_z\times\mathbf{e}_x \quad (4)$$

Here $\mathbf{e}_x$, $\mathbf{e}_y$, and $\mathbf{e}_z$ form an orthogonal system. The arrow denotes the direction of solar wind velocity. At low frequency (0.066 Hz) we can clearly see two peaks in the spectrum (Figures 4(a) and (c)), while at higher frequencies this component is absent at the higher power (Figure 4(b)), but a small "bump" is present at lower powers in the parallel direction (Figure 4(d)). The presence of a parallel component at low k is observed. He et al. (2011) and Podesta & Gary (2011) found a similar parallel component by measuring the magnetic helicity. However, magnetic helicity measurements do not directly give information about the power of fluctuations.

A key question we may ask is whether this component corresponds to parallel whistler waves (or, more precisely, kinetic fast waves (KFWs) when $kv_A/\Omega_p \leqslant 1$, which are right hand polarized in the plasma frame), or whether this is due to parallel ICWs. We consider the power spectrum of the fluctuations in the directions parallel and perpendicular to the field. Such a spectrum is constructed in Figure 5 through obtaining the power at maximum in the wavevector space, and the wavevector $\mathbf{k}$ at the corresponding power maximum at each sampling frequency. With the angle that the wavevector makes with the global mean field, we can plot the power spectrum in the directions parallel and perpendicular to the global mean

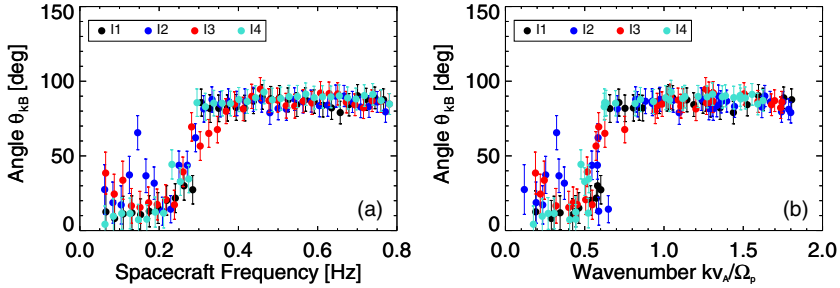

Figure 3. Propagation $\theta_{\mathbf{kB_0}}$ angles with respect to the global mean field $\mathbf{B_0}$ as a function of spacecraft frequency (a) and obtained wavenumber (b).

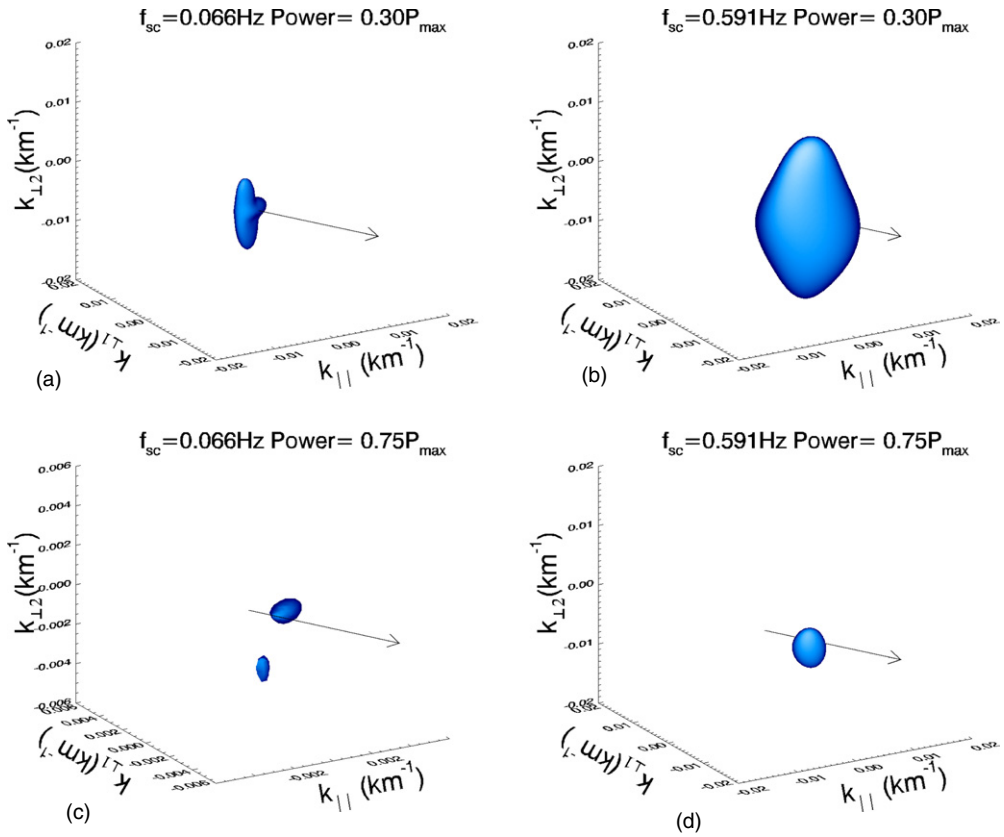

Figure 4. $P(\omega, \mathbf{k})$ obtained from k-filtering $k_\parallel$ denotes the component of the wavevector in the direction of $\mathbf{B_0}$, $k_{\perp 1}$ denotes the wavevector component in the plane of $\mathbf{B_0}$ and $\mathbf{v}_{\rm sw}$ and $k_{\perp 2} = \mathbf{k}\cdot\mathbf{e}_z$ (see Equations (2) and (3)). Isosurfaces represent areas that are over 30% of the maximum power in a and b, and over 75% of the maximum power in c and d. The left plots show a frequency of 0.066 Hz (in the region where parallel propagation angles are found) and the right plots show a frequency of 0.591 Hz (where oblique propagation angles are found). The arrows denote the average direction of the solar wind velocity.

magnetic field. The maximum power obtained from k-filtering at each sampling frequency as a function of kv_A/Ω_p is shown in Figure 5(a). The spectrum shows two power laws (Sahraoui et al. 2010b; Roberts et al. 2013).

Figures 5(b) and 5(c), show the spectrum in the parallel and perpendicular directions, respectively. The gray shaded areas are the regions where the data points are mostly from fluctuations with wavenumbers $k_\perp \gg k_\parallel$ (Figure 5(b)) or $k_\perp \ll k_\parallel$ (Figure 5(c)). In the parallel direction the spectral index is close to $-5/3$, but may be closer to -2 especially in interval 1. The small number of points and the small difference between the two scalings make it difficult to conclude that the scaling is one or the other, and difficult to rule out either of the scalings. The scalings obtained in the perpendicular direction have more points and are therefore much easier to measure, agreeing well with previous studies (Alexandrova et al. 2012; Roberts et al. 2013).

Another plasma diagnostic technique is the dispersion plot. By using the wavevector obtained from k-filtering and a measurement of the mean velocity measured by the CIS, the spacecraft frequency $\omega_{\rm sc}$ can be Doppler shifted to the plasma frame frequency $\omega_{\rm pla}$ according to $\omega_{\rm pla} = \omega_{\rm sc} - \mathbf{k}\cdot\mathbf{V}_{\rm sw}$. An error of 3.5% (Roberts et al. 2013) is assumed on the velocity determination from CIS to obtain the dispersion plot in Figure 6. It is clear that there is a large spread of values, especially at higher wavenumbers. At low wavenumbers the spread of values is much smaller; these points show a better agreement with the curve for a quasi-parallel ICW (red) than with a quasi-parallel kinetic fast (whistler) wave (blue). The sign of the frequencies and the direction of the wavevector also suggest anti-sunward waves. The sharp cutoff and the change in $\theta_{\mathbf{kB_0}}$ suggest that the fluctuations with $(kv_A/\Omega_p) < 0.6$ have different properties compared with those at $(kv_A/\Omega_p) > 0.6$. For parallel propagating whistler waves we would expect the dispersion curve to exhibit

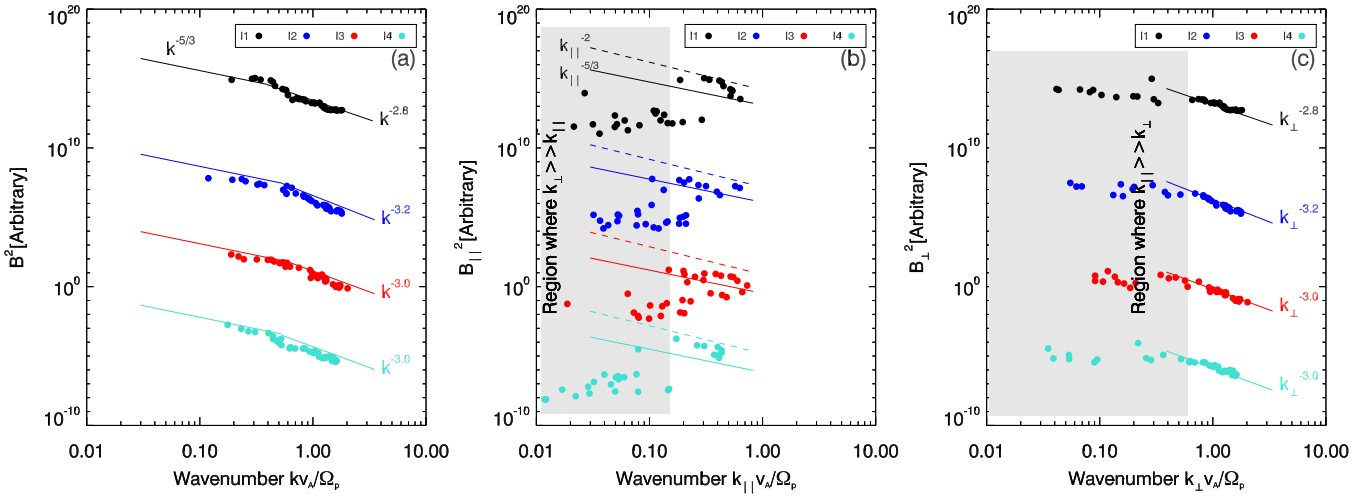

Figure 5. Power spectra of the magnetic field fluctuations in the four intervals. (a) The maximum spectral power density as a function of kv_A/Ω_p, where k is the magnitude of the wavevector at the maximum power in the wavevector space determined by the k-filtering technique. (b) The same spectral power density in (a) is shown against the parallel wavevectors $k_\parallel v_A/\Omega_p$. Two scalings of $-5/3$ (solid lines) and -2 (dashed lines) are given for comparison. The shaded area shows the region where the points are mostly populated by points where $k_\perp \gg k_\parallel$ (c) The same spectral power density in (a) is shown against the perpendicular wavevectors $k_\perp v_A/\Omega_p$. The shaded area shows the region where the points are mostly populated by points where $k_\parallel \gg k_\perp$.

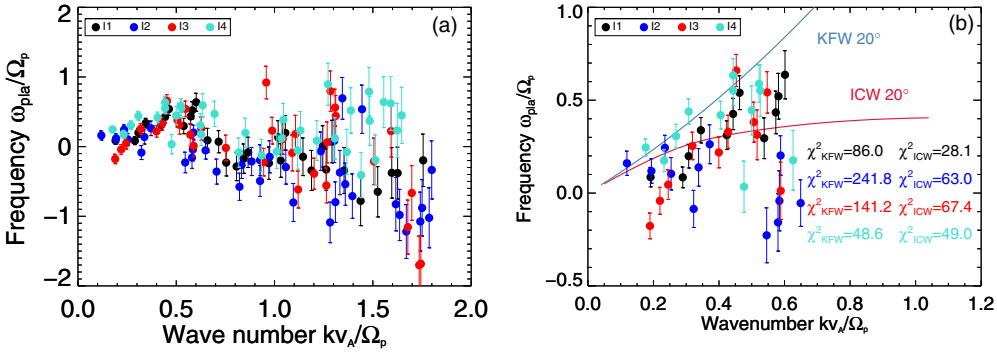

Figure 6. (a) Dispersion plots of the plasma frame frequency in the four periods studied, the error bars denote a 3.5% uncertainty in the flow speed. (b) The dispersion plot for only the parallel fluctuations along with the curve for an ion cyclotron wave (red) and a kinetic fast wave (blue) propagating at an angle of 20° to the mean field. The two theoretical dispersion curves were calculated using Vlasov theory for an electron/proton plasma with parameters similar to those in Table 1 with $T_{p\perp}/T_{p\parallel} = 1.3$, $T_{e\perp}/T_{e\parallel} = 1$, $T_{e\parallel} = 0.5T_{p\parallel}$ proton beta $\beta_p = 2k_B T_{p\parallel} n_p \mu_0/B_0^2 = 1$, and the ratio of the speed of light and the Alfvén speed equal to 2000. The χ^2 values for the four intervals are indicated with respect to both theoretical curves.

frequencies above the proton gyrofrequency at $kv_A/\Omega_p > 1$ (Li & Habbal 2001). It is noted that Perschke et al. (2013) found many data points with phase speeds much higher than that of the whistler wave. However, some of their data points could be due to aliasing because of their large phase speeds (see Section 2).

At $(kv_A/\Omega_p) > 0.6$ Figure 6 displays a large range of frequencies. At $0.6 < (kv_A/\Omega_p) < 1.3$ the frequencies ($|\omega_{\rm pla}/\Omega_p|$) are mostly low which could correspond to KAW turbulence or convected structures (Roberts et al. 2013). Figure 6(b) also displays the χ^2 (defined in Equation (5)) values for when comparing the data points to the theoretical curves for both waves. Low values of this statistic indicate a good fit of the model m_i to the data x_i which have the associated errors σ_i.

$$\chi^2 = \sum_i \frac{(x_i - m_i)^2}{\sigma_i^2} \qquad (5)$$

In all but one case (where the values are very close to each other) the χ^2 value is smaller for the ICW than for the KFW curve, suggesting that the data points agree better with the curve for the ICW. However, the values of $\chi^2 \gg 1$, which generally indicate a poor fit, suggesting that the fluctuations are poorly modeled by a single linear wave. Identifying a single exact dispersion curve is difficult, this could be due to a number of reasons both physical and in relation to the method. The spatial aliasing effect is more prevalent at higher frequencies as well as other effects such as a low signal-to-noise ratio and effects of time synchronization. If the four spacecraft are not perfectly synchronized but differ in their timing by a value of $\delta t_{\rm synch}$ this can introduce a spurious phase shift of $\omega\delta t_{\rm synch}$. Since this has a dependence on the value of ω the effect becomes more pronounced at higher frequencies. For estimation of $P(\omega_{\rm sc}, \mathbf{k})$ we require this random phase shift to be less than 5° (Pinçon & Lefeuvre 1992). Since the measured frequencies are small (mostly $\omega \lesssim \Omega_p$) and the data are analyzed to a maximum spacecraft frequency of 0.8 Hz we expect that this effect is small. It should be noted that while the estimation of k-filtering can be significantly broadened due to a low signal-to-noise ratio (S/N), the estimation is still reliable up to when S/N = 3 (Roberts 2014). However, a combination of these effects may be possible. While the effects on the method are well known individually, their combinations could lead to larger errors. Another possibility is that nonlinear physical effects (Howes & Nielson 2013) contribute to the broadening in frequency. The combination of these physical effects and instrumental uncertainties make isolating a single theoretical dispersion curve

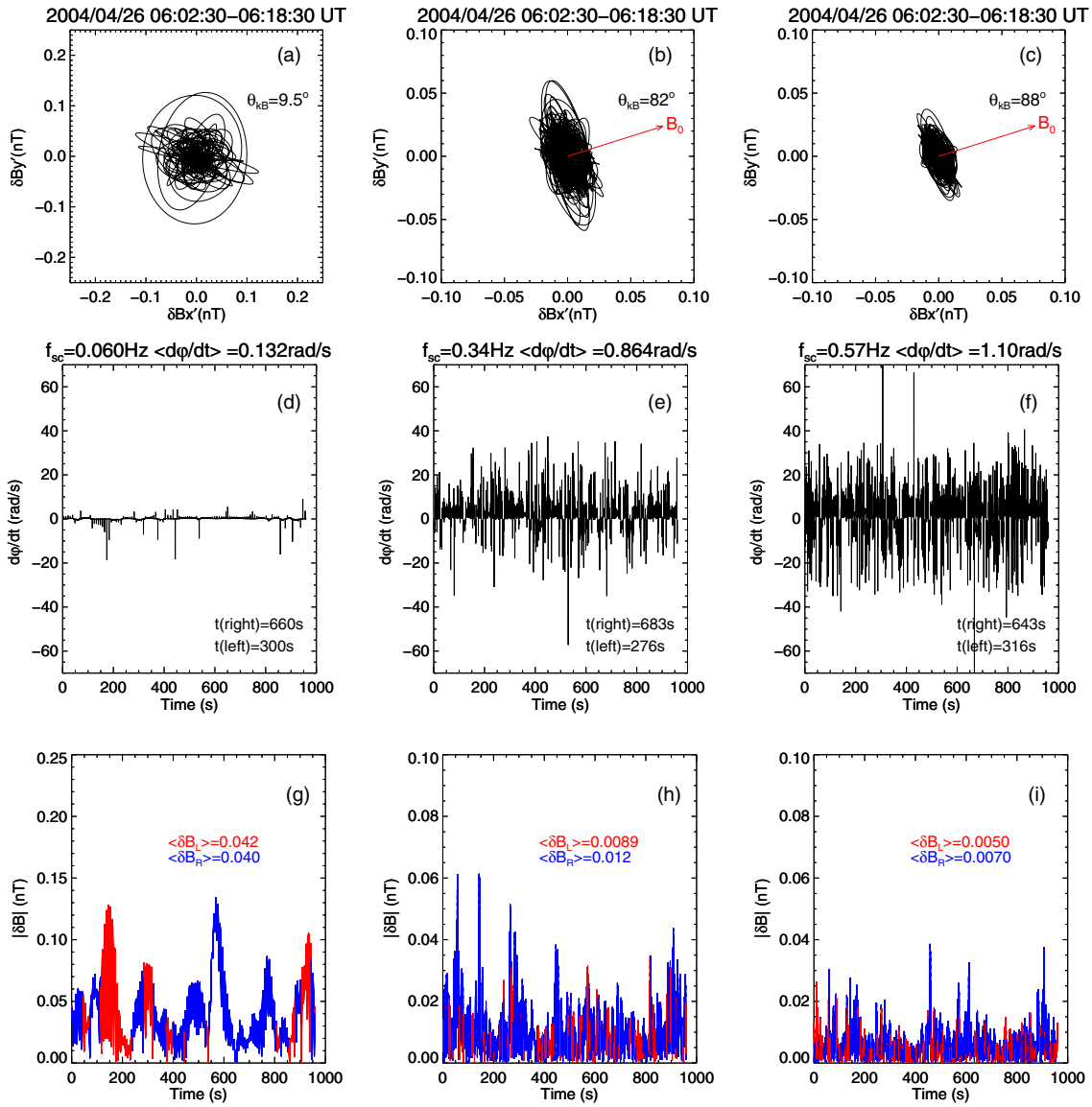

Figure 7. Top row shows hodographs in the plane perpendicular to the wavevector **k** at various spacecraft frequencies (a)0.06 Hz, (b)0.34 Hz, (c) 0.57 Hz. For the frequencies when the wavevector is oblique to the magnetic field direction the red arrow denotes the direction of the mean magnetic field. The center row shows $d\varphi/dt$ as a function of time. The bottom row shows the magnitude of δB as a function of time. Red denotes left handed polarization and blue denotes right handed polarization. Panels of the same column correspond to the same spacecraft frequency.

difficult with a limited amount of intervals. A fuller discussion of this topic as well as a statistical analysis of many intervals of the dispersion relation will be addressed in the companion paper (Roberts et al. 2015).

As a further test we consider the polarization of magnetic fluctuations in the plane perpendicular to **k**. Unlike magnetic helicity which cannot distinguish between sunward right-hand polarized kinetic fast waves and anti-sunward left-hand polarized ion cyclotron waves as they have the same signature, with the determination of the wavevector we can determine which of these waves dominates at these scales.

Here we use a wavelet transform as a natural bandpass filter (He et al. 2012a; Roberts et al. 2013) such that only a small range of frequencies are present. The wavelet transform is applied in a Cartesian coordinate system $x'y'z'$ such that $\delta B_{x'}$ and $\delta B_{y'}$ are the two magnetic field components in the plane perpendicular to **k** and that $\delta B_{z'}$ is the magnetic field component along the wavevector **k** (positive z' axis comes out of the paper). The direction of rotation is determined from the use of the $d\varphi/dt$ parameter where φ is the angle between the magnetic field vector, and the x axis, and the sign of the derivative of this with respect to time gives us the direction of rotation (Roberts et al. 2013). Negative (positive) values denote left (right) sense of rotation in this plane. The result is shown in Figure 7.

In contrast to the results presented by Roberts et al. (2013), the polarization of the low frequency component seems to be nearly circular (see Figure 7(a) for $f_{sc} = 0.06$ Hz). At higher frequencies we recover the familiar right handed elliptical polarization, with the major axis of the ellipse perpendicular to the global magnetic field direction (He et al. 2012b; Roberts et al. 2013). At $f_{sc} = 0.34$ and 0.57 Hz (Figures 7(b) and (c)), the polarization is dominantly right handed which can be attributed to kinetic Alfvén waves (Gary 1986; Roberts et al. 2013). At low frequencies the presence of dominantly right handed waves is quite puzzling; however, when **k** is close to the direction of $\mathbf{B_0}$ we would also have structures that could give left or right handed polarization. It should also be noted that at the lower frequencies $f_{sc} < 0.3$ Hz two components are resolved by the

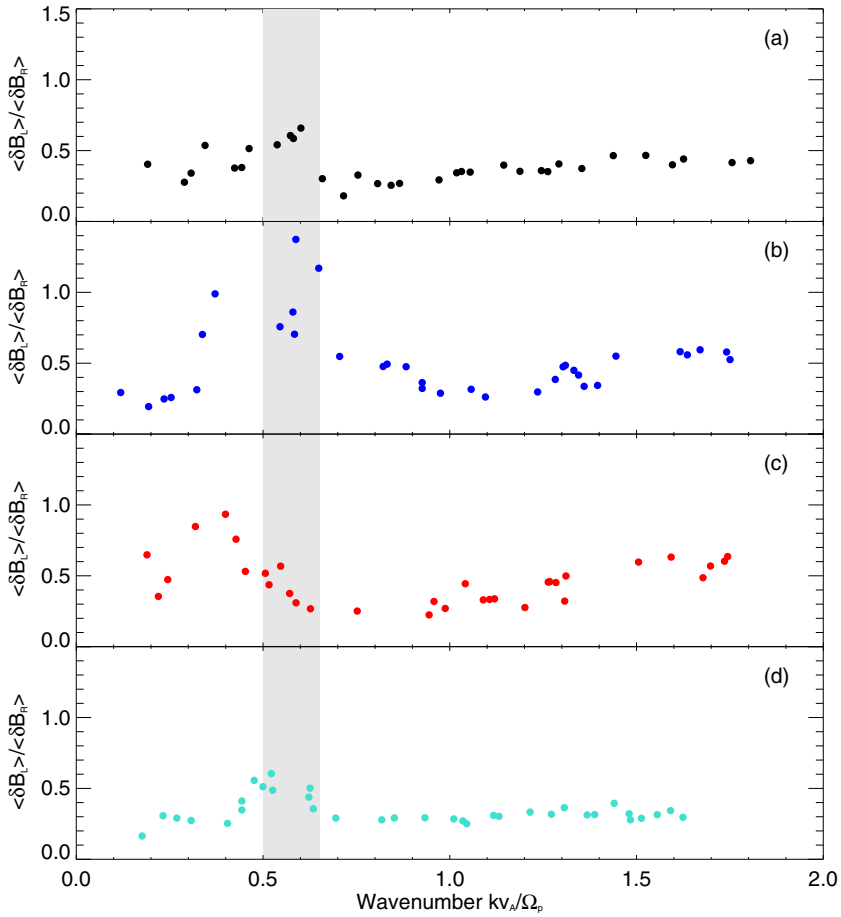

Figure 8. Polarization ratios of the magnitude of the average power of the left handed component divided by the average power of the right handed component derived from the hodographs. These plots have the same color coding as was used previously with I1 at the top and I4 at the bottom. The gray shaded area shows the region between $(kv_A/\Omega_p) = 0.5$–0.6 where we see the cutoff in the dispersion and the angle plots.

k-filtering; therefore, when using a bandpass filter we will often see a superposition of the two (or more) major components with similar power at the same spacecraft frequency, but at different wavenumbers, and this may give the appearance of a dominant right handed polarization. Shown in Figures 7(d), (e), and (f) are $d\varphi/dt$ at three frequencies. The average value of $d\varphi/dt$ are all positive, suggesting overall right handed polarization of the magnetic fluctuations. Note that $d\varphi/dt$ gives us the sense of rotation and the speed of the rotation but it does not give a complete description. For example, if there is an ICW that only exists for a short time (Jian et al. 2009, 2010), but has a large power, it would be resolved by k-filtering, but the polarization of the ICW may be overshadowed by other fluctuations that have opposite polarization but have been present for most of the time interval.

In order to better understand the polarization we plot the magnitude of the fluctuations $|\delta B| = \sqrt{\delta B_{x'}^2 + \delta B_{y'}^2}$ when they are left (red) and right handed (blue) in Figures 7(g), (h), and (i). Magnetic fluctuations with both left and right hand polarization have been observed to survive in the ion kinetic scales (Carbone et al. 2010; Narita et al. 2011; Roberts et al. 2013). To show the relative strength of fluctuations with left and right handed polarizations, we use the measurement of $d\varphi/dt$ to determine the sense of polarization. The average magnitude $\langle \delta B \rangle$ of the fluctuations with left and right handed polarizations is defined as

$$\langle \delta B_L \rangle = \frac{\int_{T_L} |\delta B| dt}{T}, \langle \delta B_R \rangle = \frac{\int_{T_R} |\delta B| dt}{T}, \quad (6)$$

where $T = T_L + T_R$ and T_L (T_R) is the total time the magnetic field fluctuations are left (right) hand polarized. The integration $\int_{T_L} dt$ ($\int_{T_R} dt$) is only done over the time when the wave polarization is left (right) handed.

In order to investigate the evolution of these powers as a function of wavenumber we investigate the ratio between the average left and right handed powers. This is given in Figure 8 for the four time intervals. Where the average power was derived from the hodograph. The ratio increases in all intervals up until around $(kv_A/\Omega_p) \sim 0.6$, (where the parallel fluctuations also disappear; Figure 3), then exhibit a sharp drop, before slowly increasing again as the wavenumber increases. It has to be noted that at $(kv_A/\Omega_p) > 0.6$ the fluctuations have $\theta_{\mathbf{kB_0}} \sim 90^\circ$, the existence of KAWs and structures make the polarization complex (Roberts et al. 2013).

As a further test, to better understand the differences between the oblique component, the magnetic helicity (He et al. 2011; Podesta & Gary 2011) will be investigated. The helicity as defined by Matthaeus & Goldstein (1982) is given below.

$$\sigma_M = kH'_m(k)/E_B(k). \quad (7)$$

Here k is the reduced wavenumber (where k is along the measurement direction), H'_m is the reduced wavenumber-dependent fluctuating magnetic helicity, and E_B is the trace of the magnetic power spectrum. The polarization analysis suggests that left handed fluctuations are present and have high powers, but what we may be seeing is the superposition of this component

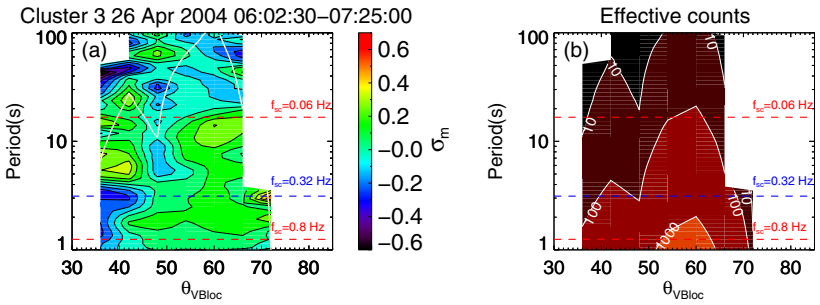

Figure 9. (a) shows the angle (between bulk velocity and local magnetic field) dependence of the magnetic helicity σ_m as a function of waveperiod for the interval 06:02:30-07:25:00UT. Bluer areas represent negative helicity, and lighter areas represent positive helicity, white areas represent no data. (b) shows the distribution of effective counts again as a function of angle and waveperiod, the contours are spaced logarithmically with the values 10, 100, 1000, and 10,000 indicated on the contours. The contour line (white) of 20 is plotted in (a) to indicate regions that the magnetic helicity measurements are less reliable.

and the oblique component as well as fluctuations from coherent structures (which could be left or right handed). From Figure 6 it is clear that most points on the dispersion plot (both parallel and oblique) are anti-sunward propagating (positive frequency in the plasma frame, or within the error estimation of being positive). From a total of 139 data points 76 have positive frequencies, 63 have negative frequencies. While a total of 93 data points are either positive or within error limits of being positive. For ICWs we would expect the helicity signature to be opposite to that of the oblique component. We assume that short periods when the Cluster is connected to the foreshock do not significantly affect the helicity in the interval since these are for brief periods. Taylor's hypothesis is also assumed since we plot the helicity as a function of angle between the local mean magnetic field $\mathbf{B}_{\rm loc}$ and the bulk velocity $\mathbf{v}_{\rm sw}$. Here we use the same definition given by Podesta & Gary (2011) to calculate the local mean field $\overline{\mathbf{B}}_s(t_n)$ on the scale of s at time t_n:

$$\overline{\mathbf{B}}_s(t_n) = \frac{1}{A_s}\sum_{t_m=t_n-3s}^{t_n+3s}\mathbf{B}(t_m)\exp\left\{-\frac{(t_m-t_n)^2}{2s^2}\right\}, \quad (8)$$

where the scale s is used in the wavelet transform and A_s is given by

$$A_s = \sum_{t_m=t_n-3s}^{t_n+3s}\exp\left\{-\frac{(t_m-t_n)^2}{2s^2}\right\} \quad (9)$$

We then look at how the magnetic helicity varies as the angle between the local magnetic field and the solar wind velocity changes. Practically the angular dependence of the magnetic helicity is given below.

$$\sigma_M = \frac{2\left\langle Im\left[\tilde{B_T}(s,t_n)\tilde{B_N}^*(s,t_n)\right]\right\rangle_{\theta_a<\theta<\theta_b}}{\langle|\tilde{B_R}(s,t_n)|^2+|\tilde{B_T}(s,t_n)|^2+|\tilde{B_N}(s,t_n)|^2\rangle_{\theta_a<\theta<\theta_b}}. \quad (10)$$

where R, T, and N denote radial, tangential, and normal components of the magnetic field B. When performing the helicity analysis we will use RTN coordinates, in order to be consistent with previous studies. Any quantity with a tilde (~) denotes the wavelet transform at scale s, the θ denotes the angle between the local magnetic field and the velocity vectors, and the angled brackets $\langle ...\rangle$ denote an average for quantity with the local mean magnetic field lying in the angular interval $\theta_a < \theta < \theta_b$. In this study we use bins of width 6°.

While the angular dependence of magnetic helicity has typically been used for long data intervals of the order of 10 ~ 20 hr in the cases of He et al. (2011) and Podesta & Gary (2011). We are limited to short intervals due to the Cluster's orbit, and can only sample the solar wind not connecting to the foreshock for very short periods, i.e., much shorter than that used in the two studies mentioned previously. However, since strict requirements of stationarity are not required we can relax data requirements and select the whole interval from 06:02:30-07:25:30 UT. It is important to note that this time interval contains a period when connected to the bow shock, while we would like to eliminate this it does also limit the variation of angles we can sample if we break our already short time series into smaller sub intervals. The helicity spectrum is shown in Figure 9(a), we can see a region of positive magnetic helicity expected for an outward magnetic sector ($B_R > 0$) (He et al. 2011). We also see a signature of *opposite* helicity being centered close to $f_{\rm sc} = 0.32$ Hz with a small distribution either side this could be interpreted as a signature of ICWs. Along with the magnetic helicity we plot the number of effective counts in a bin $n_{\rm eff} = (n\Delta t/P)$ where P is the period of the scale of interest and n is the actual number of data points that contribute to the bin. This gives an estimate of how reliable the helicity measurement is in each bin. We notice that the most counts are centered around $\theta_{\mathbf{vB}_{\rm loc}} = 60°$, near the edges and for larger periods there are fewer effective counts. This makes our estimation at angles far away from $\theta_{\mathbf{vB}_{\rm loc}} = 60°$ and at long periods less reliable. This is likely due to the short data interval analyzed, and the fact that the $\theta_{\mathbf{vB}_{\rm loc}}$ does not vary much in the short data period.

4. DISCUSSION

This work has revealed the presence of a component of magnetic fluctuations propagating quasi-parallel to the mean magnetic field direction in the solar wind in the intervals studied, in addition to a perpendicular component. The co-existence of the two populations has been shown by magnetic helicity measurements (He et al. 2011; Podesta & Gary 2011; Klein et al. 2014) and 2D power spectral density derived from spatial correlation function (He et al. 2013). These studies have used single spacecraft data. This parallel component has been quite elusive and has not previously been resolved by the k-filtering. We suggest that this is due to the fact that the parallel component is typically dominated by the perpendicular component, and this intrinsic property coupled with the projection effect discussed make this component difficult to resolve. The four intervals studied here constitute a very rare data sample where $\mathbf{B_0}$ points in a favorable direction for recovery of the parallel component. Of a statistical study performed using the k-filtering technique, only the 4 intervals presented here out of a total of 52 can recover a parallel component (see the companion paper by Roberts et al. 2014b, or Roberts 2015). We are also restricted due to limitations

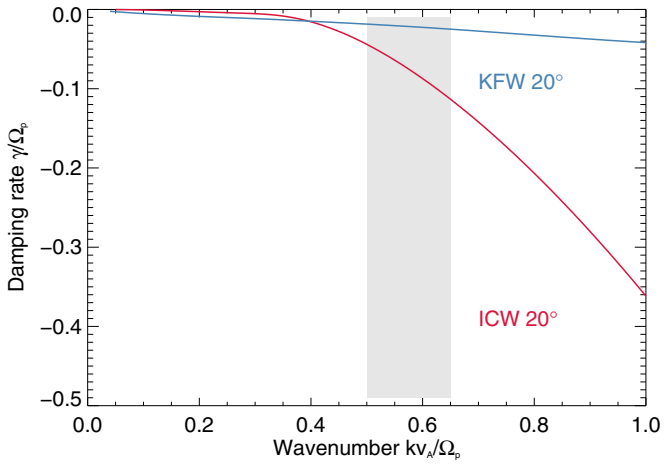

Figure 10. Linear damping rates (the imaginary part of the complex frequency) obtained from Vlasov theory for an ICW (red) and a whistler wave (blue) propagating at an angle of 20° to the global mean field for an electron/proton plasma with $T_{p\perp}/T_{p\parallel} = 1.3$, $T_{e\perp}/T_{e\parallel} = 1$, $T_{e\parallel} = 0.5T_{p\parallel}$ and the proton beta is $\beta_p = 2k_B T_{p\parallel} n_p \mu_0 / B_0^2 = 1$ and the ratio of the speed of light and the Alfvén speed is 2000. Here it is assumed that the velocity distribution of protons is bi-Maxwellian. The gray shaded area denotes the same region of wavenumbers where we see a sharp cutoff in the dispersion, angle and polarization ratio plots.

of the method, such as spacecraft geometry requirements that make usable data difficult to find.

The propagation angles show that there is a parallel component that exists from low wavenumbers to wavenumbers around $(kv_A/\Omega_p) \sim 0.6$ where the component disappears abruptly. This could be due to kinetic effects coming into play. Quasi-parallel ICWs at these scales are expected to undergo significant damping. Figure 10 shows the damping curves from linear Vlasov theory for ICWs and for parallel whistler waves assuming that the velocity distribution of protons is bi-Maxwellian (Li & Habbal 2000). The shaded region shows where we see the sharp cutoff, and this agrees well with an increase in the damping rate observed for ICWs, while the damping rate for the whistler wave remains fairly constant at the scales of interest. Therefore, the sharp cutoff observed near $(kv_A/\Omega_p) \sim 0.6$ is more likely to be characteristic of an ICW rather than a whistler wave. If there is a parallel cascade present then damping could occur at each step in the cascade (Podesta et al. 2010), so the total damping would be much greater. Nonlinear interactions may also affect the damping rates. However, the linear damping rates and the sharp cutoff near the start of the dissipation range suggest that the ICWs are heavily damped and could be responsible for proton and heavy ion heating, and for observed features in the helium and proton velocity distribution functions (Marsch et al. 1982b, 1982a).

Analysis of the dispersion relation shows that these waves are propagating in the anti-sunward direction, with the curves agreeing well with those for parallel ICWs. The other possibility for explaining the helicity observed by He et al. (2011) and Podesta & Gary (2011) is parallel whistler waves propagating in the sunward direction. We interpret the data as indicative of ICWs rather than whistler waves for the following reasons: the direction obtained from *k*-filtering is in the anti-sunward direction, and the frequency in the plasma frame is also positive for most points, and also lower than the proton gyrofrequency. The turbulence at higher wavenumbers transitions to being dominantly perpendicular, and the data points are quite scattered which can be caused by number of factors such as inaccuracies in the velocity measurement, low S/N at higher spacecraft frequencies, or due to a physical effect resulting from Alfvén wave collisions such as discussed by Howes & Nielson (2013). However, most of the points above $(kv_A/\Omega_p) \sim 0.6$ are close to $\omega \sim 0$, in accordance with expectations for KAW turbulence (Sahraoui et al. 2010b), or for a combination of KAW turbulence and coherent structures (Roberts et al. 2013). The majority of these data points are either positive or within error limits of being positive. For these waves we would expect a right hand polarization in the plane perpendicular to **k** and a positive magnetic helicity signature.

At high frequencies in the plane perpendicular to **k** dominant elliptical polarization can be seen, which supports the KAW interpretation (Gary 1986; Roberts et al. 2013). At lower frequencies the polarization seems to be closer to circular, and both left and right handed polarizations are seen: when we look at the magnitudes of these fluctuations the amount of power in the left and right handed fluctuations is quite similar. The ratio of the powers of the left handed to right handed fluctuations increases with wavenumber. We speculate that this could be due to quasi-parallel waves being generated at a range of wavenumbers $(kv_A/\Omega_p < 1)$ as a result of a kinetic plasma instability in places of closer to the Sun than the orbit of the Earth. Another possible explanation is that these waves were originally generated in the foreshock region where the solar wind is magnetically connected to the bow shock. Back streaming particles from the bow shock can readily generate waves in the kinetic regime. Those non-parallel propagating waves including Alfvén waves in the kinetic regime will be able to propagate and carry energy into nearby solar wind regions not directly connected to the bow shock. In addition to these possibilities, projection effects due to the quasi-oblique component and random senses of polarization due to structures may also contribute to the polarization seen. After coming to a peak value this quantity exhibits a sharp dip, which we interpret as damping of ICWs. Hence we suggest that the increase in left handed polarization is caused by an instability acting at a certain wavenumber range, then this component is damped at small scales by cyclotron resonance. The helicity analysis supports this idea, with opposite helicities recovered for the oblique and the parallel components. There is also a region of positive helicity that is quasi parallel at lower frequencies. This has also been observed in Figure 3 of Podesta & Gary (2011) but has not been thoroughly discussed. This could be due to a small component of parallel whistler waves; however, we are limited in our angular range due to the short interval. This limitation is especially prevalent near the edges at large angles from the mean angle between the magnetic field and the velocity. Another key limitation is that we are restricted to using Taylor's hypothesis, and assume that **k** is along $\mathbf{v}_{\rm sw}$. This hypothesis is not necessarily accurate (Howes et al. 2014; Klein et al. 2014). In fact at small wavenumbers the deviation of **k** from the direction of the flow ($\theta_{\mathbf{kv}_{\rm sw}}$) can be as large as ∼40° as is shown in Table 2. The helicity analysis in itself is not conclusive and has its limitations; however, it does provide complementary information to the other data presented here, and shows that the senses of polarization for the quasi-parallel and quasi-oblique components indeed have opposite polarization.

Following the sharp decrease there is a slow increase in this quantity, which we propose is due to a different mechanism, such as an increase in the amount of sunward waves with wavenumber (see companion paper Roberts et al. 2014b). One could argue that the right handed polarization is a signature of whistler waves; however, it is difficult to conclude that these waves dominate over the ICWs. The power of the left handed

fluctuations is significant, and effects from the other waves present in the signal at a given frequency can contribute to the right handed sense of polarization observed. It is of course possible that parallel sunward whistler waves also coexist but are dominated by the ICWs and the perpendicular KAWs. Coherent structures could also be present and would also contribute to the polarization observed.

The source of this parallel component has been suggested to be either due to a parallel cascade that is slower and less efficient than the perpendicular cascade (He et al. 2011), or to a temperature anisotropy instability (Podesta & Gary 2011; Klein et al. 2014). The importance of the parallel component to the development of the solar wind turbulence is being debated (He et al. 2012a; Klein et al. 2014) due to the inability for the magnetic helicity measurements alone to determine the power of the parallel component.

The temperature anisotropy present in the data (Table 1) is too small to generate plasma instability if bi-Maxwellian velocity distribution is assumed. No obvious ion beams in the ion velocity distribution function measured from the CIS-HIA instrument can be seen (not shown). One possibility is that these parallel waves are generated upstream of 1 AU, in accordance with the findings of Jian et al. (2009, 2010) where the ICWs are suggested to have been generated closer to the Sun than 0.3 AU, possibly by a temperature anisotropy instability (Podesta & Gary 2011).

5. CONCLUSION

We have used the *k*-filtering method in the fast solar wind and have been able to detect a parallel propagating population which we interpret as ion cyclotron waves. The dispersion plot suggests that these are more characteristic of ICWs than KFWs, and are also mostly propagating in the anti-sunward direction. The magnetic helicity analysis confirms that these two populations have the *opposite* polarization. These analyses complement each other well and support the interpretation that these parallel fluctuations are ICWs rather than KFWs. These waves are shown to exist up to about $(kv_A/\Omega_p) \sim 0.6$ where we suggest they experience strong damping, and cannot cascade further below proton scales. We have discussed a limitation of the *k*-filtering technique, indicating that the angle between the velocity and the magnetic field may favor the recovery of perpendicular fluctuations. Polarization of these fluctuations in the plane perpendicular to **k** and the dispersion plot suggest that the parallel component is dominated by ion-cyclotron waves and not parallel whistler waves, although we cannot rule out the presence of a small component of parallel whistler waves. These waves are likely to originate from a region closer to the Sun than 1 AU, since we cannot observe a local signature in the proton velocity distribution function.

REFERENCES

Alexandrova, O., Lacombe, C., Mangeney, A., Grappin, R., & Maksimovic, M. 2012, ApJ, 760, 121
Alexandrova, O., Saur, J., Lacombe, C., et al. 2009, PhRvL, 103, 165003
Antonucci, E., Abbo, L., & Telloni, D. 2012, SSRv, 172, 5
Balogh, A., Carr, C., Acuna, M., et al. 2001, AnGeo, 19, 1207
Belcher, J. 1971, ApJ, 168, 509
Bieber, J., Chen, J., Matthaeus, W., Smith, C., & Pomerantz, A. 1993, JGRA, 98, 3585
Biskamp, D., Schwarz, E., & Drakem, J. 1996, PhRvL, 76, 1264
Bourouaine, S., Alexandrova, O., Marsch, E., & Maksimovic, M. 2012, ApJ, 749, 102
Bruno, R., & Carbone, V. 2013, LRSP, 10, 2
Bruno, R., Carbone, V., Sorriso-Valvo, L., & Bavassano, B. 2003, JGR, 108, 1130
Bruno, R., & Trenchi, L. 2014, ApJL, 787, L24
Bruno, R., Trenchi, L., & Telloni, E. 2014, ApJL, 793, L15
Carbone, V., Perri, S., Yordanova, E., et al. 2010, PhRvL, 104, 181101
Chen, C., Boldyrev, S., Xia, Q., & Perez, J. C. 2013, PhRvL, 110, 225002
Coroniti, F. V., Kennel, C. F., Scarf, F. L., & Smith, E. J. 1982, JGR, 87, 6029
Cranmer, S. R. 2014, ApJS, 213, 16
Décréau, P. M. E., Fergeau, P., Krasnoselskikh, V., et al. 2001, AnGeo, 19, 1241
Escoubet, C., Fehringer, M., & Goldstein, M. 2001, AnGeo, 19, 1197
Etcheto, J., & Faucheux, M. 1984, JGR, 89, 6631
Gary, S. 1986, JPlPh, 35, 431
Gary, S., Montgomery, M., Feldman, W., & Forslund, D. 1976, JGR, 81, 1241
Gary, S. P., & Smith, C. 2009, JGR, 114, 1
Glassmeier, K., & Neubauer, F. 1993, JGR, 98, 20921
Goldreich, P., & Sridhar, S. 1995, ApJ, 438, 763
Goldreich, P., & Sridhar, S. 1997, ApJ, 20, 680
He, J., Marsch, E., Tu, C.-Y., Yao, S., & Tian, H. 2011, ApJ, 731, 85
He, J., Tu, C.-Y., Marsch, E., & Yao, S. 2012a, ApJL, 745, L8
He, J., Tu, C.-Y., Marsch, E., & Yao, S. 2012b, ApJ, 749, 86
He, J., Tu, C., Marsch, E., Bourouaine, S., & Pei, Z. 2013, ApJ, 773, 72
Hollweg, J. V., & Isenberg, P. A. 2002, JGRA, 107, A7
Howes, G., Klein, K. G., & TenBarge, J. M. 2014, ApJ, 789, 106
Howes, G., & Nielson, K. D. 2013, PhPl, 20, 072302
Jian, L. K., Russell, C. T., Luhmann, J. G., et al. 2009, ApJ, 701, L105
Jian, L. K., Russell, C. T., Luhmann, J. G., et al. 2010, JGR, 115, A12115
Klein, K., Howes, G., & TenBarge, J. M. 2014, ApJL, 789, L20
Klein, K., Howes, G., TenBarge, J. M., & Podesta, J. J. 2014, ApJ, 785, 138
Kohl, J., Noci, G., Antonucci, E., et al. 1998, ApJ, 1, 127
Lacombe, C., Mangeney, A., & Harvey, C. 1985, JGR, 90, 73
Lengyel-Frey, D., Hess, R., MascDowall, R., et al. 1996, JGR, 101, 27555
Li, H., Gary, S., & Stawicki, O. 2001, GeoRL, 28, 1347
Li, X., & Habbal, S. 1999, SoPh, 190, 485
Li, X., & Habbal, S. 2001, JGR, 106, A6
Li, X., Habbal, S., Kohl, J., & Noci, G. 1998, ApJL, 501, L133
Li, X., & Habbal, S. R. 2000, JGR, 105, 27377
Marsch, E., Mühlhäuser, K., Rosenbauer, H., Schwenn, R., & Neubauer, F. 1982a, JGR, 87, 35
Marsch, E., Mühlhäuser, K., Schwenn, R., et al. 1982b, JGR, 87, 52
Matthaeus, W., & Goldstein, M. 1982, JGR, 87, 10347
Matthaeus, W., Goldstein, M., & Roberts, D. A. 1990, JGR, 95, 20673
Narita, Y., Gary, S. P., Saito, S., Glassmeier, K., & Motschmann, U. 2011, GeoRL, 38, L5101
Neubauer, F., Musmann, G., & Dehmel, G. 1977, JGR, 82, 3201
Perri, S., Carbone, V., & Veltri, P. 2010, ApJ, 725, L52
Perri, S., Goldstein, M. L., Dorelli, J. C., & Sahraoui, F. 2012, PhRvL, 109, 191101
Perschke, C., Narita, Y., Gary, S. P., Motschmann, U., & Glassmeier, K.-H. 2013, AnGeo, 31, 1949
Pinçon, J., & Lefeuvre, F. 1991, JGR, 96, 1789
Pinçon, J., & Lefeuvre, F. 1992, JATP, 54, 1237
Podesta, J. 2013, SoPh, 286, 529
Podesta, J., Borovsky, J., & Gary, S. P. 2010, ApJ, 712, 685
Podesta, J. J., & Gary, S. P. 2011, ApJ, 734, 15
Reme, H., Aoustin, C., Bosqued, J. M., et al. 2001, AnGeo, 19, 1303
Robert, P., Roux, A., Harvey, C., et al. 1998, in Tetrahedron Geometric Factors, in Analysis Methods for Multi-Spacecraft Data, chap. 13, ed. P. Paschmann & G Daly (Noordwijk: ESA Publications Division), 323
Roberts, O. W. 2014, PhD thesis, Aberystwyth Univ.
Roberts, O. W., Li, X., & Jeska, L. 2014, GI, 3, 247
Roberts, O. W., Li, X., & Jeska, L. 2015, ApJ, 802, 2
Roberts, O. W., Li, X., & Li, B. 2013, ApJ, 769, 58
Sahraoui, F., Belmont, G., Goldstein, M., & Rezeau, L. 2010a, JGR, 115, 1
Sahraoui, F., Goldstein, M., Belmont, G., Canu, P., & Rezeau, L. 2010b, PhRvL, 105, 131101
Sahraoui, F., Huang, S., & Patoul, J. D. 2013, arXiv:1303.7394v2
Salem, C., Howes, G., Sundkvist, D., et al. 2012, ApJ, 745, L9
Shebalin, J., Matthaeus, W., & Montgomery, D. 1983, JPlPh, 29, 525
Stawicki, O., Gary, S., & Li, H. 2001, JGR, 106, 8273
Taylor, G. I. 1938, RSPSA, 164, 476
Telloni, D., Antonucci, E., & Doedero, M. A. 2007, A&A, 476, 1341
Tjulin, A., Pinçon, J.-L., Sahraoui, F., Andre, M., & Cornilleau-Wehrlin, N. 2005, JGR, 110, 1
Tu, C.-Y., & Marsch, E. 1995, SSRv, 73, 1
Tu, C.-Y., & Marsch, E. 1997, SoPh, 1712, 363
Verscharen, D., Marsch, E., Motschmann, U., & Müller, J. 2012, PhPl, 19, 022305